

Prediction of supersonic jet noise from complex nozzles

By J. W. Nichols, F. E. Ham, S. K. Lele AND P. Moin

1. Motivation and objectives

This project is motivated by the growing need for innovative strategies to reduce the noise produced by high-performance supersonic aircraft. The aeroacoustic phenomenon of jet noise, intricately connected to the turbulence dynamics in the jet shear layers and in the region downstream of the jet potential core, remains a large component of the overall noise generated by supersonic aircraft, despite significant scientific investigation as to its cause. While jet noise reducing techniques have some application in the design of traditional subsonic commercial aircraft, jet noise is a problem especially for supersonic aircraft that are typically powered by low-bypass turbofan engines. The large velocity ratio and the presence of shocks in the exhaust plume from low-bypass engines cause jet noise to be the dominant component of the overall aircraft noise, and therefore is an important issue in the design of the next generation of civil supersonic transport.

Jet noise reduction technology also has application in the design of high-performance tactical aircraft. Jet noise is of particular concern on aircraft carriers, where it is necessary for deck crew to be in relatively close proximity to the aircraft at takeoff and landing. In such harsh acoustic environments (150 dB), even the most advanced hearing protection cannot provide complete long-term protection from permanent hearing loss (NRAC, 2009). Additionally, noise reduction techniques have the potential for significant benefit in regions where communities and airfields serving supersonic aircraft are in close proximity. In these increasingly common situations, deployment of effective sound reduction technology would minimize complaints and aid in compliance with noise regulations.

Large-eddy simulation (LES) coupled to a Ffowcs Williams-Hawkings (FWH) solver has emerged as a useful tool for the prediction of jet noise (Bodony & Lele 2008). To investigate jet noise reduction strategies with LES, the need to simulate complex geometries is clear. Current jet noise reduction techniques include the addition of tabs or chevrons to the nozzle rim (Liu *et al.* 2009), alteration of the cross-sectional shape of the nozzle (Tam 1998; Tam & Zaman 2000), beveling of the nozzle exit (Viswanathan *et al.* 2008), and the addition of an array of micro-jets around the nozzle perimeter (Alkisar *et al.* 2007; Shur *et al.* 2010). In each case, significant three-dimensional structure is added to the nozzle geometry. Previous approaches to the treatment of 3D geometry include utilization of multi-block structured grids (Spalart & Shur 2009), the general grid interface (GGI) technique (Burak *et al.* 2009), and the immersed boundary method (Du & Morris 2011). Unstructured LES, however, is ideally suited to resolving complex geometry with body-fitted meshes, and for this reason, unstructured finite-element simulations based on the MILES technique (Liu *et al.* 2009) have been used previously. The unstructured finite volume LES solver “CharLES” developed at Cascade Technologies, Inc. takes a different approach, however, by introducing numerical stencils based on higher-order polynomial expansion to limit dissipation. The purpose of this brief is to assess the capability of the

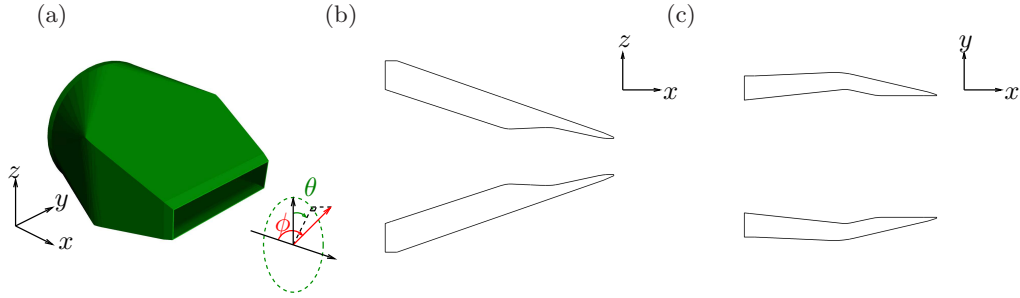


FIGURE 1. Rectangular nozzle geometry: (a) 3D view of nozzle exterior; (b) mid-plane cross section along minor axis; (c) mid-plane cross section along major axis.

CharLES unstructured LES solver for the aeroacoustic prediction of supersonic jets from complex nozzles.

2. Results

In order to demonstrate the capability of fully unstructured LES (coupled to an FWH solver) to accurately predict the noise produced by jets issuing from nozzles of arbitrarily complex geometry, we consider two test cases. For validation purposes, these cases correspond exactly to actual nozzle geometries used in experimental acoustic testing by James Bridges et al. at the NASA Glenn Research Center. In particular, we will consider underexpanded supersonic jets issuing from a plain rectangular nozzle as well as a rectangular nozzle with chevrons.

2.1. Heated rectangular jet

The first test case involves a plain rectangular nozzle of aspect ratio 4:1, shown in Figure 1(a). The entire flow in and around the nozzle is simulated, in addition to the jet plume downstream. The interior surface of the nozzle gradually transforms from a circular cross section upstream to a rectangular cross section at its exit, while undergoing a complicated sequence of contractions and expansions as shown in cross sections shown in Figures 1(b) and 1(c). The contractions and expansions in the two cross-stream directions offset one another, however, so that the cross-sectional area decreases monotonically from inlet to exit, producing an underexpanded supersonic jet plume downstream.

The 4:1 plain rectangular jet was simulated at both isothermal (setpoint 9020) and heated (setpoint 9050) operating conditions. Both operating conditions used a nozzle pressure ratio (NPR) of $P_0/P_\infty = 3.18$, where P_0 and P_∞ are the stagnation pressures inside the nozzle and in ambient fluid, respectively. This NPR yields a jet Mach number $M_j = u_j/c_j = 1.4$, where u_j and c_j are the jet velocity and the speed of sound at fully expanded conditions within the jet core. The two operating points differed in the nozzle temperature ratio (NTR) T_0/T_∞ defined in terms of stagnation temperatures inside the nozzle, T_0 , and in the freestream, T_∞ . Note that $NTR > 1$ for the isothermal condition accounts for the natural cooling as the flow accelerates from the stagnation condition. For the heated case, the elevated NTR results in a hot jet inside which the speed of sound c_j is also elevated. For a constant M_j , this implies that u_j is also greater than in the isothermal case. This can be seen by defining an acoustic Mach number $M_a = u_j/c_\infty$ in terms of the free stream speed of sound c_∞ .

To assess the quality of the LES solutions, each operating condition was simulated

Setpoint	M_j	M_a	P_0/P_∞	T_0/T_∞
9020	1.4	1.4	3.180	1.391
9050	1.4	1.8	3.153	2.300

TABLE 1. Operating conditions for the supersonic rectangular nozzle. The setpoint name matches the nomenclature of Bridges & Wernet (2008).

Setpoint	Grid cells	Δx_{noz}	Duration
9020	11M	0.03h	200h/ u_j
9020	45M	0.03h	100h/ u_j
9020	86M	0.03h	100h/ u_j
9050	11M	0.03h	200h/ u_j
9050	293M	0.01h	100h/ u_j

TABLE 2. Series of rectangular jet simulations utilizing different mesh resolutions for the two operating condition given in Table 1.

using a range of mesh resolutions, from a coarse mesh of ≈ 11 million control volumes (11M c.v.'s) to a fine mesh of 293M c.v.'s (see Table 2). The physical extent of the computational domain was identical in all cases, and characteristic boundary conditions were used at all inflow and outflow boundary conditions. To further avoid unphysical reflections produced by the turbulent plume crossing the outlet boundary, a numerical sponge layer was incorporated just upstream, the strength and shape of which were determined using the guidelines outlined in Mani (2012). For all cases, the Reynolds number $Re = u_j D_e / \nu = 150,000$, and the Vreman (2004) model was used to represent the effect of subgrid scale motions. ν is the kinematic viscosity and D_e is the equivalent diameter of the rectangular jet, defined as the diameter of a circular jet with the same exit area. Purely hexahedral meshes were used for all simulations.

Chronologically, the 11M and 86M isothermal jets were simulated first. The 86M mesh was formed simply by subdividing each hexahedron in the 11M mesh into eight smaller hexahedrons. Both the 11M and 86M meshes contained a degree of axial grid stretching in the downstream regions away from the nozzle. It was found that this gradual loss of axial resolution and increase in mesh anisotropy in the downstream regions led to anomalous humps in the mid-frequencies of the far-field noise spectra (Nichols *et al.* 2011). This effect was especially apparent at upstream and lateral observer locations. A similar effect was observed by Bogey *et al.* (2011) for round jets. To remedy this problem, we took advantage of the fully unstructured nature of the CharLES solver, and adaptively refined the 11M mesh to yield an nearly isotropic mesh in the downstream regions. The near-nozzle resolution was left unchanged, however, yielding a mesh containing 45M c.v.'s. The 45M adapted mesh completely eliminated the spurious mid-frequency noise, and in this way out-performed the even larger 86M mesh. At high frequencies, however, the 86M mesh still performed better than the other two, because of the additional resolution provided in the near-nozzle regions. The heated jet was first simulated on an identical 11M mesh, but then, using the lessons learned from the isothermal cases, a new 293M mesh was constructed using adaptive refinement (see Figure 2) in such a way so as to yield

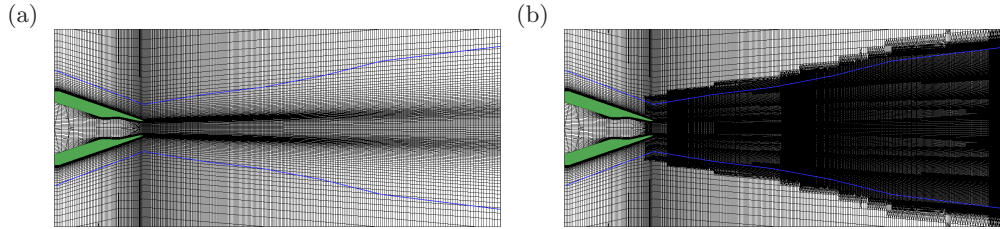


FIGURE 2. Near-nozzle visualization of the meshes used in the (a) 11M and (b) 293M simulations. The 293M mesh was created by adaptively refining the region inside the FWH surface (blue).

downstream isotropy as well as near-nozzle refinement. The isothermal jet simulations have been presented elsewhere (Nichols *et al.* 2011), so for the purposes of this brief, we focus solely upon the heated case.

Figure 3 provides a flow visualization of the heated rectangular jet taken from a snapshot of the 293M mesh simulation. In the top frame, contours of temperature are shown on the $y = 0$ plane, with gray and yellow indicating the cold and hot extremes, respectively. Because the jet is underexpanded as it leaves the nozzle, a train of shock cells form downstream of the nozzle. In the isothermal jet, these shock cells were observed to oscillate in the z -direction in connection with a strong screech tone. For the heated case, no such oscillatory mode was observed and, as we will see, the screech tone was largely absent in this simulation.

Frames (A-F) of Figure 3 show the three-dimensional development of the rectangular jet on a sequence of radial cross sections taken at locations indicated by the corresponding labeled vertical dashed lines in the top frame. As noted by Zaman (1996, 1999), a turbulent rectangular jet spreads faster along its minor axis than along its major axis. In this way, the jet gradually transforms from a rectangular cross section to a circular cross section as it evolves downstream.

The solid cyan lines show the location of the FWH surface used for acoustic post-processing. For the post-processing we use a variant of the FWH equation proposed by Spalart & Shur (2009) in which only pressure and velocity are recorded along the surface, and then the density is computed *a posteriori*. In heated jets, this allows for a more aggressive placement of the FWH surface with respect to the turbulent regions because pressure is a more uniform function than density. In addition to using the density-substituted FWH variant, we also mitigate the spurious sound produced by vorticity passing through the surface by averaging over a series of 16 end-caps, following Shur *et al.* (2005) and Mendez *et al.* (2009). In Figure 3, the end-caps are represented by the solid vertical cyan lines. The dashed vertical cyan line indicates the beginning of the sponge layer.

Figure 4 shows the computed farfield spectra for the heated jet. The left panel shows spectra taken at an upstream angle ($\phi = 60^\circ$), the center panel corresponds to the lateral ($\phi = 90^\circ$) angle, and the right panel to a downstream angle ($\phi = 150^\circ$). Here, the angle ϕ is taken with respect to the upstream jet axis with an origin located at the center point of the nozzle exit plane. Likewise, θ indicates the azimuthal direction with $\theta = 0^\circ$ and $\theta = 90^\circ$ aligned with the narrow and wide dimensions of the nozzle, respectively. In Figure 4, the red and blue curves represent the 11M and 293M mesh simulations, respectively, and are compared to experimental measurements (black). As the resolution increases, the spectra align increasingly well with the experimental measurements, suggesting that the unstructured LES methodology is indeed capturing all of the relevant physics of the

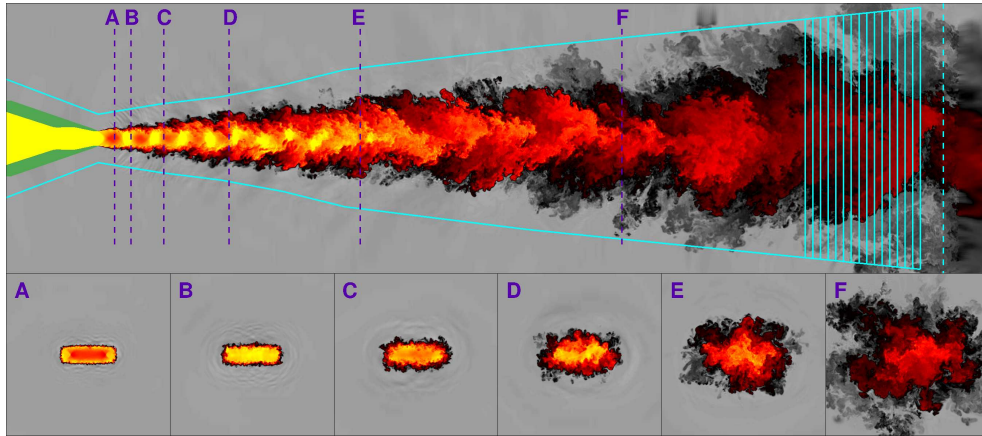


FIGURE 3. Instantaneous temperature contours for the heated supersonic jet (SP9050) from the plain 4:1 rectangular nozzle.

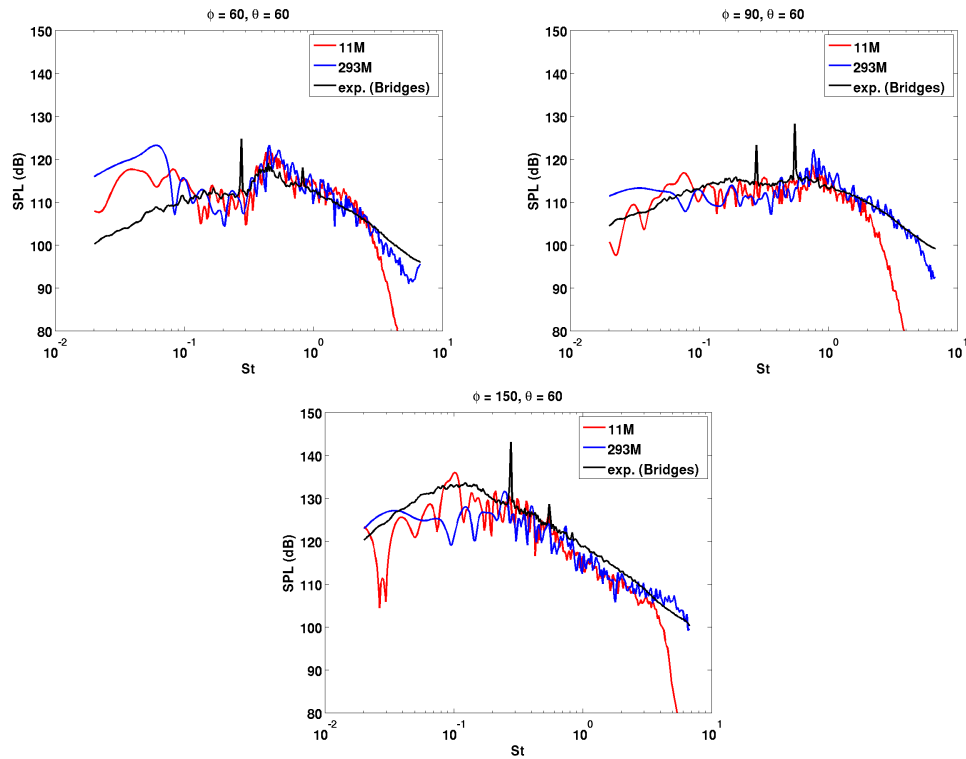


FIGURE 4. Farfield spectra for the heated supersonic jet. Spectra computed from the coarse and fine simulations are shown by the red and blue curves, respectively. For comparison, noise spectra measured from James Bridges’ experiment are given by the black curves.

problem. In particular, the broadband shock associated noise is clearly visible in the $\phi = 60^\circ$ plot as the peaky spectrum centered around $St = 0.5$. We should note that while the simulations provide access to entire spatial data fields, they usually cover a shorter time interval than realizable in experiment. For this reason, the task of obtaining

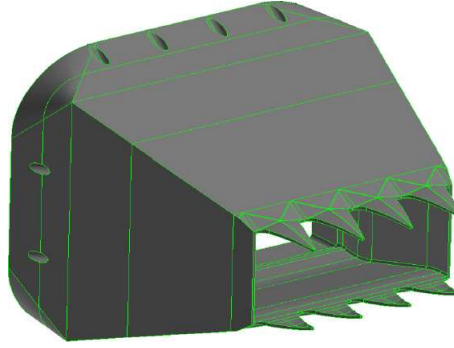


FIGURE 5. Rectangular nozzle geometry with chevrons, matching that of experimental nozzle NA2C3 developed at the NASA Glenn Research Center.

converged statistics at the low frequency end of the spectrum becomes a challenge for simulations. The breakdown in convergence at very low frequencies gives rise to the discrepancies in Figure 4. We expect that these discrepancies may be remedied by running the simulations longer, albeit at considerable computational expense.

2.2. Rectangular jet with chevrons

Figure 5 shows the NA2C3 rectangular chevron nozzle developed for experimental testing at the Small Hot Jet Acoustic Rig (SHJAR) facility at the NASA Glenn Research Center. This nozzle was developed as part of the “Extensible Rectangular Nozzle Model System” used to investigate the effects of nozzle aspect ratio, chevrons, and bevels on high-speed jet noise production (Frate & Bridges 2011). This nozzle has aspect ratio 2:1 (no 4:1 aspect ratio nozzles were designed with chevrons), and four large chevrons are attached to each of its long edges. The chevrons arc into the issuing flow and impart significant streamwise vorticity to it.

For simulation, the precise nozzle geometry was supplied by James Bridges at the NASA Glenn Research Center in the form of a Computer-Aided Design (CAD) file. The computational domain, including the volume inside the nozzle and extending downstream to a distance of 30 equivalent diameters, was discretized by a series of progressively fine meshes, ranging from 6 million to 262 million control volumes. All of the meshes contained purely hexahedral elements, body-fitted to the surface described by the CAD file. As before, the coarse mesh was created first, and then adaptively refined, clustering grid points isotropically inside the FWH surface according to Nichols *et al.* (2011). Characteristic boundary conditions were used at all inflow and outflow boundaries, together with a numerical sponge layer at the outlet.

The operating conditions for the chevron jet simulations performed to date correspond to SP9020 (Table 1). For these cases, the Reynolds number $Re \approx 1.5 \times 10^6$. Like the plain rectangular nozzle, the chevron jet nozzle is also purely convergent, and so produces an underexpanded jet containing shocks. To capture the effects of these shocks, a hybrid-ENO scheme (Khalighi *et al.* 2011) was employed with a switch based on the magnitude of the local dilatation. The high-resolution cases were run as part of a 60 million cpu-hour ALCC allocation on the IBM BlueGene/P machine at the Argonne National Laboratory. The CharLES code was found to scale nearly ideally to as many as 65,536 processors.

Figure 6 shows a snapshot of the turbulent flow from the fine scale (263M) simulation. In the top frame, contours of temperature are shown using a white-to-black-to-yellow color scale on an axial cross section taken near to one of the nozzle’s lips (not the center

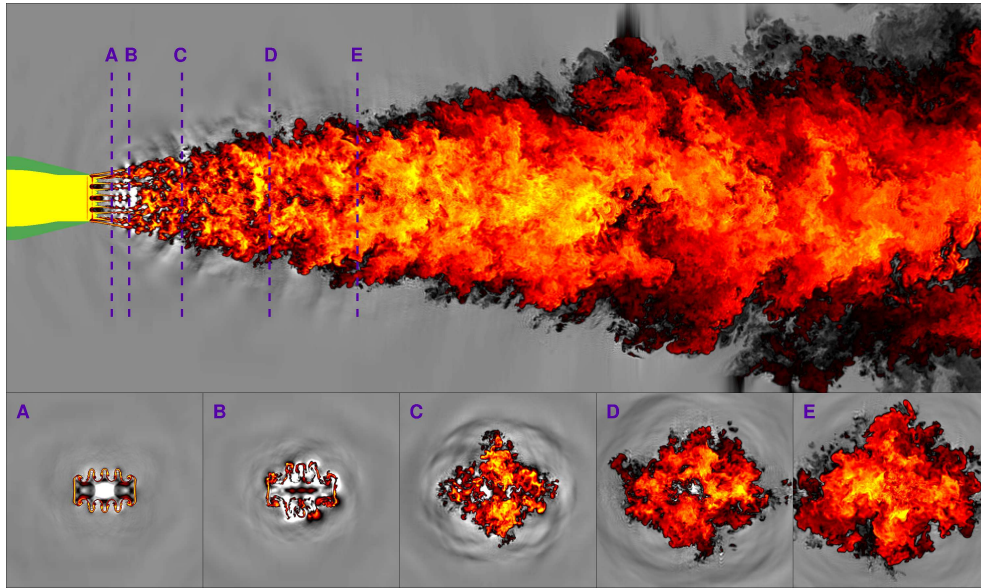


FIGURE 6. Instantaneous temperature contours from the 263M mesh simulation of the rectangular chevron nozzle. The nozzle material is shown in green.

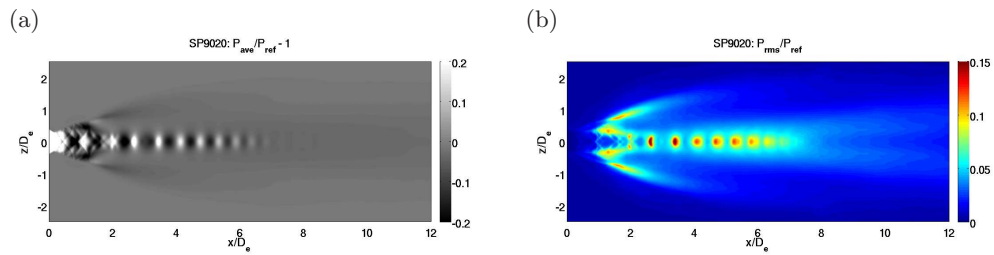


FIGURE 7. (a) Mean and (b) RMS pressure statistics on a center plane cutting through the narrow dimension of the chevron nozzle for SP9020.

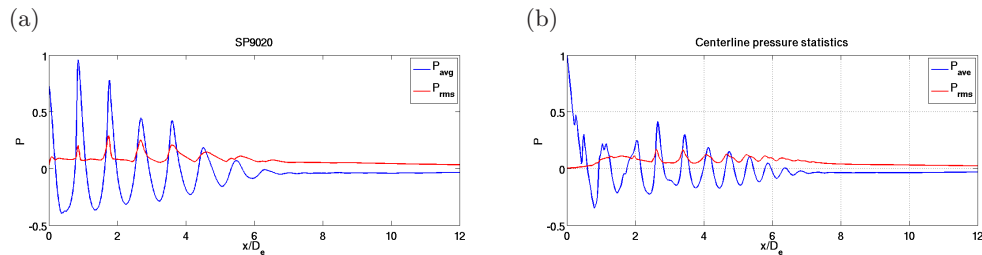


FIGURE 8. Pressure statistics measured along the jet axis for (a) the plain rectangular jet and (b) the rectangular jet with chevrons.

plane). The four chevrons are visible as wedge shapes (the nozzle material is shown in green) as they arc through this plane and down into the flow. Radial cross sections are shown in the bottom frames, corresponding to the vertical dashed lines in the top frame. Because the jet is underexpanded, three side jets are propelled outwards between the chevrons along both the upper and lower edges of the nozzle. These side jets merge

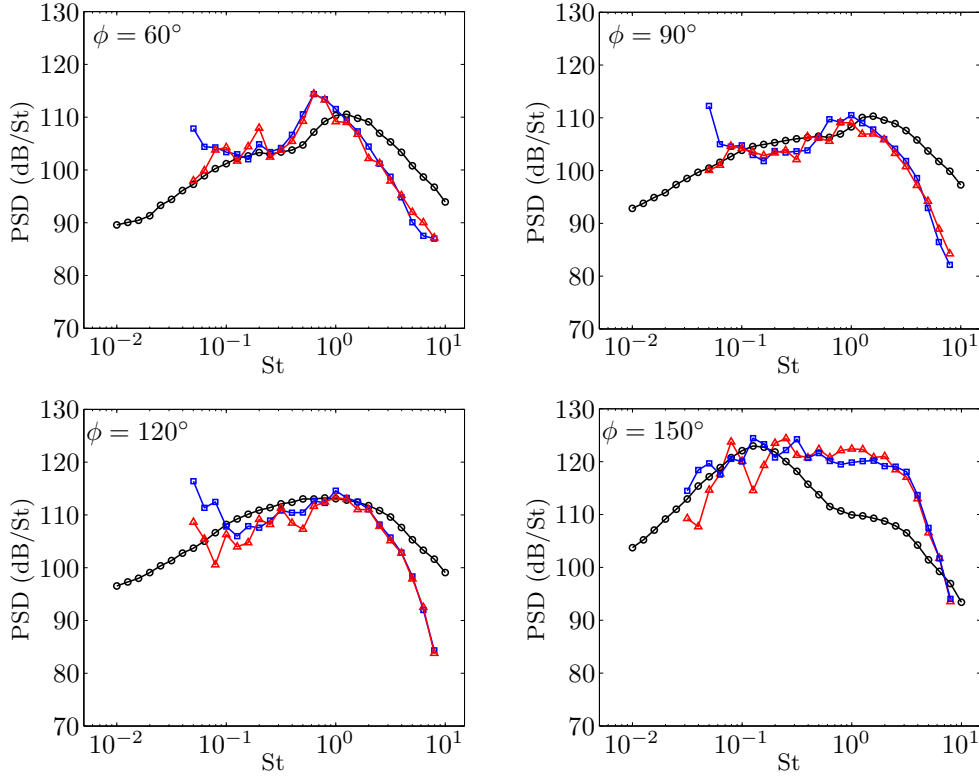


FIGURE 9. Farfield noise spectra from chevron simulations: 90M LES (blue) and 263M LES (red) compared to experiment (black).

together to form a plus-shaped cross section further downstream, near to the collapse of the potential core. This downstream region is known to be a sensitive region for the production of the peak acoustic radiation.

Figure 7 shows that the chevrons affect the near-nozzle jet flow in two ways important to noise production. In this figure, the mean and RMS pressure statistics are shown on a center cross section slicing through the narrow dimension of the nozzle. First, the RMS pressure reveals that the side jets enhance turbulent mixing in regions away from the jet axis. Second, the mean pressure field reveals a multitude of shocks in the near-nozzle region. These shocks are generated at both the chevron tips and the troughs in between them. The net result is that the highly organized shock cells in a plain rectangular jet (Figure 8(a)) are broken up into many small shock cells in the chevron rectangular jet (Figure 8(b)). In this way the chevron jet expands in many small steps instead of in a relatively few large steps.

Figure 9 shows farfield spectra for the chevron jet taken at four different angles ϕ from the upstream jet axis. The blue and red curves represent the farfield spectra computed from the 90M and 263M mesh simulations, respectively. The black curves show the third-octave spectra measured from experiment. While the shapes of the computed spectra are somewhat similar to the shapes obtained experimentally, the agreement in this case is not as good as that obtained for the plain rectangular jet. In particular, the simulations

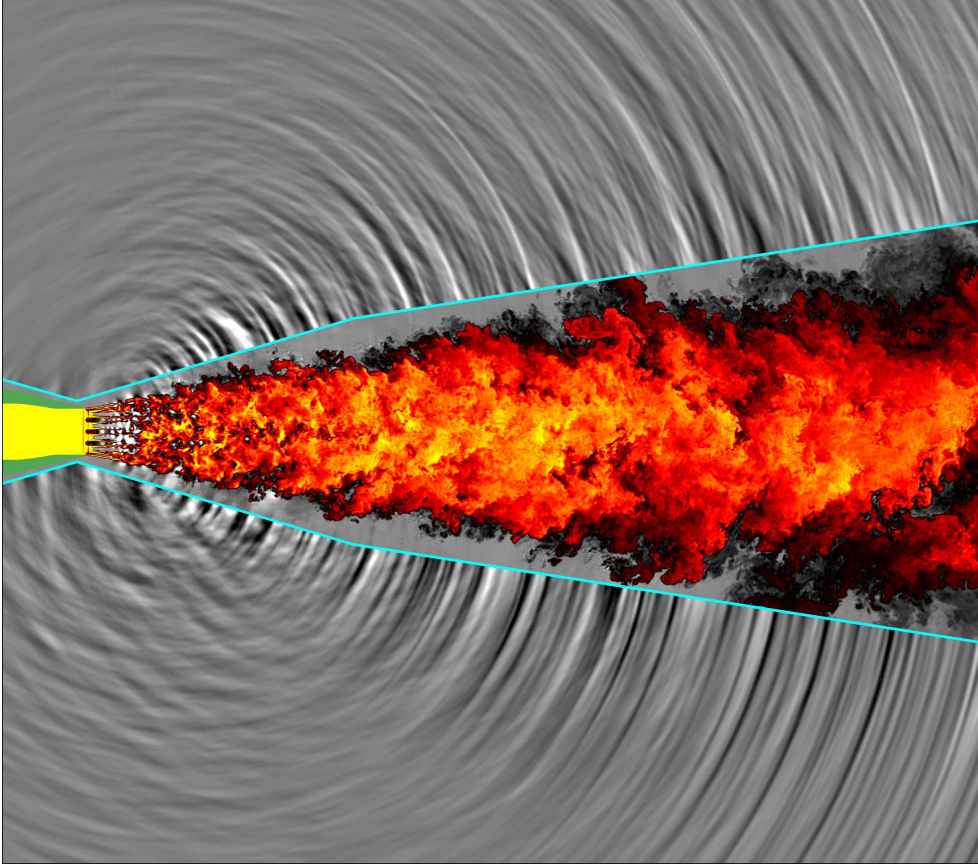


FIGURE 10. A visualization of the sound projected losslessly from the FWH surface (cyan), in relation to the turbulence which generated it (chevron jet). Redscale contours of temperature are displayed inside the FWH surface, while grayscale contours represent the perturbation pressure in the exterior region.

underpredict the high-frequencies at $\phi = 60^\circ, 90^\circ, 120^\circ$ but significantly overpredict them for $\phi = 150^\circ$. Unfortunately, refining the mesh did not seem to help.

One difference between the plain and chevron simulations was that the chevron mesh was generated from a much more coarse initial mesh, before refining. This led to a sharper transition at the fine-coarse interface just outside of the FWH surface. The effects of this interface can be seen in Figure 6, where the sound waves emanating from the turbulence are quickly damped as they reach this interface. By carefully placing the FWH surface in the zone between the turbulence and the mesh coarsening, however, we can recover the acoustic waves as they would appear if no damping had taken place. This FWH sound is shown in relation to the turbulence in Figure 10.

In addition to damping incident acoustic waves, the fine-coarse mesh interface may also produce reflections, which may explain some of the high-frequency discrepancies in the farfield spectra. Because the FWH surface is angled, acoustic waves with $\phi = 60^\circ, 90^\circ, 120^\circ$ arrive at the interface at a high angle of incidence, and thus are likely to reflect back through the FWH surface. At 150° , the waves may have a glancing reflection, and thus pile up downstream. For the chevron jet, much of the omni-directional sound is

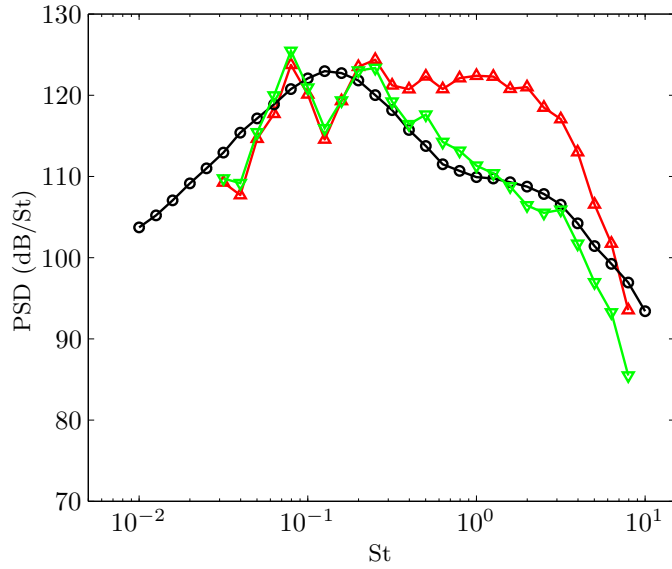


FIGURE 11. Farfield spectra for chevron jet at $\phi = 150^\circ$: experimental measurements (black), 263M LES simulation with full FWH surface (red), 263M LES simulation with FWH surface starting at $x = 6D_e$ (green).

produced by the broadband shock associated noise in the vicinity of the nozzle. Figure 11 removes the near-nozzle portions from the FWH surface, computing the noise only from the downstream portions. The resulting spectrum shows that most of the noise responsible for the high-frequency discrepancy is indeed generated in this near-nozzle region.

3. Conclusions and future plans

In this brief, we have demonstrated that the farfield sound predictions obtained from the fully unstructured LES solver CharLES, coupled with an FWH solver, converge well to the experimental results for a heated supersonic jet issuing from a plain rectangular nozzle. The adaptive mesh capability afforded by the unstructured solver was crucial in the development of a mesh which efficiently captures turbulence as the jet undergoes a fully three-dimensional transition from rectangular to circular cross section. The unstructured mesh also allowed for the addition of chevrons along two edges of the nozzle lip in the second test case considered. While the chevron jet simulation produced farfield noise spectra of similar shape and amplitude to those measured from experiment, larger discrepancies were observed, especially in the mid- to high-frequency range of the downstream directed sound. Removal of the near-nozzle portion of the FWH integration surface, however, corrected this discrepancy, suggesting more resolution is needed close to the nozzle lip to capture the complicated three-dimensional transition to turbulence in this region. Another difference between the plain rectangular jet simulations and the chevron jet simulations was the transition between fine and coarse resolution just outside the FWH surface. The more abrupt transition in the case of the chevron jet could lead to unphysical reflections, which may corrupt the FWH surface data. To remedy these

issues, we have adaptively refined the fine mesh to cluster more grid points close to the nozzle lip, and have applied a strategy to smooth the fine-to-coarse mesh transitions, incorporating several layers of intermediate-sized cells between the two regions. The resulting mesh contains 528M c.v's and is currently running on 131,072 processors of the Argonne BlueGene/P machine, and further results are eagerly awaited.

Acknowledgments

The authors gratefully acknowledge support from NASA grant #NNX07AC94A and from the Predictive Science Academic Alliance Program at Stanford University. We are also grateful to I. Bermejo-Moreno of CTR for his careful reading of a preliminary version of this manuscript and for his comments which have helped improve it greatly. Computational resources were provided by a DoD Challenge project allocation at the ERDC and AFRL supercomputer centers, and an ALCC computer allocation at Argonne National Laboratories.

REFERENCES

- ALKISLAR, M. B., KROTHAPALLI, A. & BUTLER, G. W. 2007 The effect of streamwise vortices on the aeroacoustics of a mach 0.9 jet. *J. Fluid Mechanics* **578**, 139–169.
- BODONY, D. J. & LELE, S. K. 2008 Current status of jet noise predictions using large-eddy simulation. *AIAA Journal* **46** (2), 364–380.
- BOGEY, C., MARSDEN, O. & BAILLY, C. 2011 Large-eddy simulation of the flow and acoustic fields of a reynolds number 10^5 subsonic jet with tripped exit boundary layers. *Physics of Fluids* **23**, 035104.
- BRIDGES, J. & WERNET, M. 2008 Turbulence associated with broadband shock noise in hot jets. AIAA Paper 2008–2834.
- BURAK, M. O., ERIKSSON, L.-E., MUNDAY, D., GUTMARK, E. & PRISELL, E. 2009 Experimental and numerical investigation of a supersonic C-D chevron nozzle. AIAA Paper 2009-4004.
- DU, Y. & MORRIS, P. J. 2011 Noise simulations of supersonic hot jets for chevron nozzles. AIAA Paper 2011-2787.
- FRATE, F. C. & BRIDGES, J. E. 2011 Extensible rectangular nozzle model system. AIAA Paper 2011-975.
- KHALIGHI, Y., NICHOLS, J. W., BRES, G., HAM, F. E., LELE, S. K. & MOIN, P. 2011 Unstructured large-eddy simulation for prediction of noise issued from various nozzles. In *Proceedings of the 17th AIAA/CEAS Aeroacoustics Conference*.
- LIU, J., KAILASANATH, K., RAMAMURTI, R., MUNDAY, D., GUTMARK, E. & LOHNER, R. 2009 Large-eddy simulations of a supersonic jet and its near-field acoustic properties. *AIAA Journal* **47** (8), 1849–1864.
- MANI, A. 2012 Analysis and optimization of numerical sponge layers as a nonreflective boundary treatment. *J. Computational Physics* **231** (2), 704–716.
- MENDEZ, S., SHOEBY, M., SHARMA, A., LELE, S. K. & MOIN, P. 2009 Post-processing of large-eddy simulations for jet noise predictions. *Center for Turbulence Research Annual Research Briefs* pp. 17–31.
- NICHOLS, J. W., HAM, F. E. & LELE, S. K. 2011 High-fidelity large-eddy simulation for supersonic rectangular jet noise prediction. AIAA Paper 2011-2919.

- SHUR, M. L., SPALART, P. R. & STRELETS, M. K. 2005 Noise prediction for increasingly complex jets. part i: methods and tests. *International Journal of Aeroacoustics* **4**, 213–246.
- SHUR, M. L., SPALART, P. R. & STRELETS, M. 2010 LES-based evaluation of a microjet noise reduction concept in static and flight conditions. In *Proceedings of the IUTAM Symposium on Computational Aero-Acoustics for Aircraft Noise Prediction*. Elsevier Ltd.
- SPALART, P. R. & SHUR, M. L. 2009 Variants of the Ffowcs Williams - Hawkings equation and their coupling with simulations of hot jets. *International Journal of Aeroacoustics* **8** (5), 477–491.
- TAM, C. K. W. 1998 Influence of nozzle geometry on the noise of high-speed jets. *AIAA Journal* **36** (8), 1396–1400.
- TAM, C. K. W. & ZAMAN, K. B. M. Q. 2000 Subsonic jet noise from nonaxisymmetric and tabbed nozzles. *AIAA Journal* **38** (4), 592–599.
- VISWANATHAN, K., SHUR, M., SPALART, P. R. & STRELETS, M. 2008 Flow and noise predictions for single and dual-stream beveled nozzles. *AIAA Journal* **46** (3), 601–626.
- VREMAN, A. W. 2004 An eddy-viscosity subgrid-scale model for turbulent shear flow: Algebraic theory and applications. *Physics of Fluids* **16**, 3670.
- ZAMAN, K. B. M. Q. 1996 Spreading characteristics and thrust of jets from asymmetric nozzles. AIAA Paper 96–0200.
- ZAMAN, K. B. M. Q. 1999 Spreading characteristics of compressible jets from nozzles of various geometries. *J. Fluid Mechanics* **383**, 197–228.